INTERNATIONAL JOURNAL OF PRECISION ENGINEERING AND MANUFACTURING Vol. 16, No. 11, pp. 2271-2279 OCTOBER 2015 / 2271
DOI: 10.1007/s12541-015-0292-x ISSN 2234-7593 (Print) / ISSN 2005-4602 (Online)

Design of a Flexure-based Auto-Focusing Device for a Microscope

Yilin Liu[1] and Qingsong Xu[1,#]

1 Department of Electromechanical Engineering, Faculty of Science and Technology, University of Macau, Avenida da Universidade, Taipa, Macau, China
Corresponding Author / E-mail: qsxu@umac.mo, TEL: +853-8822-4278, FAX: +853-8822-2426

KEYWORDS: Compliant mechanism, Flexure hinge, Micropositioning, Long stroke, Auto-focusing

This paper presents the design, fabrication, and testing procedures of a compliant auto-focusing device for a microscope. To obtain a long focusing range, a new flexure positioning mechanism is devised based on multi-stage leaf springs. The proposed device allows a precise focusing without friction and backlash effects. A voice coil motor is employed to drive the positioning mechanism. The stiffness model and resonant-frequency model are developed analytically. These models are employed for an architectural optimization of the mechanism parameters to maximize the resonant frequency under the driving stroke and force constraints. The performance of the designed flexure mechanism is validated through finite-element analysis (FEA) simulation investigations. Results show that the positioning mechanism enables a long focusing range over 10 mm with a resonant frequency higher than 50 Hz, which allows an auto-focusing operation with rapid response. Moreover, a prototype is fabricated for experimental studies. LabVIEW software with Vision Development Module is adopted for image processing in the auto-focusing process. By employing the standard deviation of the image grayscale as the criterion of focusing, an exhaustive search method is used to determine the focusing point. Experimental results demonstrate the effectiveness of the developed auto-focusing device.

Manuscript received: February 9, 2015 / Revised: May 7, 2015 / Accepted: August 21, 2015

1. Introduction

As the development and advance of micro science and technology, auto-focusing microscopes are replacing manual ones in more and more fields. The reason lies in that auto-focusing system enables the automation of imaging process. Moreover, it can reduce the influence of focusing error imposed by manual operation. Typical applications range from robotic cell micromanipulation and imaging[1-3] to scanning probe microscopy (SPM) and nanolithography,[4-6] etc. Majority of the existing auto-focusing devices are based on a DC motor, which drives the microscope to move in the focusing-axis direction.[7,8] However, traditional rigid bearing based guiding mechanisms suffer from the adverse effects of backlash and friction. Such effects cause a positioning error hence a focusing error of the device.

To cater for the increased requirement on accuracy and precision in auto-focusing microscope, flexure-based compliant mechanisms can be adopted.[9-11] Unlike traditional mechanisms, flexure mechanisms produce motion by making use of the elastic deformation of the material. Hence, flexure mechanisms allow the elimination of backlash and friction problems and enable an improvement on positioning accuracy. In the literature, several flexure mechanisms have been reported for the auto-focusing of microscopes. For example, a small sized actuator with compliant mechanism is proposed in Ref. 12, which is free of friction. As a result, the open-loop control becomes possible and the performance of optical image stabilization is improved. In addition, a new auto-focusing device with a flexure hinge and a voice coil motor (VCM) is proposed for mobile imaging devices in Ref. 13. By using flexure mechanism, the serious friction problems and weaknesses of conventional mechanisms due to the misalignment of driving force and guiding axis of the supporting mechanism are overcome. However, the displacement of the existing flexure mechanisms is restricted by the yield strength of the material, which limits the focusing range of the device. Hence, the main challenge is how to achieve a large focusing range using flexure mechanisms.

Generally, to achieve a large positioning displacement, the flexure can be made with longer length and smaller width. However, the physical size is constrained by the compactness requirement. In order to realize a long-stroke positioning while maintaining a compact physical size, the concept of multistage compound parallelogram flexure (MCPF) has been proposed in the literature.[14] In this research, the idea of MCPF is

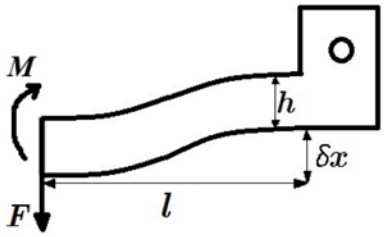

Fig. 1 Combined deformation of a beam element

extended to devise a conceptual design of a microscope auto-focusing device with long focusing range. Considering the potential of VCM in auto-focusing applications,[15,16] a VCM is employed for the actuation of the device in this research. Both analytical modeling and finite element analysis (FEA) simulations are carried out to illustrate the new design. Moreover, a prototype is fabricated for experimental testing by realizing suitable focusing algorithms.

The main contribution of this work is the design of a new electromechanical device for auto-focusing of a digital microscope and the validation of the conceptual design using experimental investigations. The remaining parts of the paper are organized as follows. Section 2 presents the mechanism design process. Analytical modeling and optimum design are dictated in Section 3. Section 4 reports on static and dynamic simulation study of the device. Prototype fabrication and performance testing is conducted in Section 5. Experimental study of the developed auto-focusing device is detailed in Section 6. Section 7 concludes this paper.

2. Flexure Positioning Mechanism Design

One role of the positioning mechanism is to support the microscope. In order to obtain a clear image from the microscope, sufficient displacement should be provided for the positioning mechanism to move in the axial direction. The design goal of this range is ±5 mm in this work. So, the desired total stroke is 10 mm.

2.1 Flexure hinge selection

To realize the design objective, a suitable flexure hinge is selected first. It is known that there are two popular types of flexure hinges. One is notched hinge, and the other one is beam element, i.e., leaf flexure. Both types have been widely employed in flexure mechanism design.[17,18] Generally, the former is able to provide a relatively accurate motion with small shift value of the rotation center. However, due to the stress concentration, only a small magnitude of motion can be provided. In contrast, the latter is capable of large-stroke motion with the same length of flexure. Hence, the leaf flexure is adopted in this research to achieve a long focusing range.

Acting as a fixed-guided beam, the deformation of a leaf flexure is shown in Fig. 1. The free end suffers from a force F and a moment M. The combination of F and M produces the "S" shape of deformation as shown in Fig. 1.

Due to the combined effect, the rotation angles at the two terminals are equal to each other, and the displacement is the difference between them. It can be easily derived that

$$0 = \frac{Fl^2}{2EI} - \frac{Ml}{EI} \tag{1}$$

$$\delta_x = \frac{Fl^3}{3EI} - \frac{Ml^2}{2EI} \tag{2}$$

where E is the modulus of elasticity of the material and I represents the moment of inertia.

Then, solving the above two equations yields

$$F = \frac{2M}{l} \tag{3}$$

$$\delta_x = \frac{Fl^3}{12EI} \tag{4}$$

Because the deformation is bidirectional, the total displacement is $\Delta x = 2\delta_x$. It follows from Eqs. (3) and (4) that

$$\Delta x = 2\delta x = \frac{Ml^2}{3EI} \tag{5}$$

In the next step, the expression of the moment M is derived. The moment M can be calculated from the stress formula, which is shown below

$$\sigma_{max} = \frac{M_{max} y}{I} = \frac{M_{max} \frac{h}{2}}{I} \tag{6}$$

$$M_{max} = \frac{\sigma_{max} bh^2}{6} \tag{7}$$

where $I = (bh^3)/12$ and σ_{max} is the allowable stress of the material.

Substituting Eq. (7) and $I = (bh^3)/12$ into Eq. (5) leads to

$$\Delta x_{max}^{single} = \frac{2\sigma_{max} l^2}{3hE} \tag{8}$$

A multi-stage compound parallelogram flexure (MCPF) is constructed by multiple leaf springs. Its motion range and stiffness can be expressed by

$$\Delta x_{max}^{multi} = \frac{2N\sigma_{max} l^2}{3hE} \tag{9}$$

$$K_{multi} = \frac{Ebh^3}{Nl^3} \tag{10}$$

where N is the number of basic module of compound parallelogram flexure. More details about MCPF can be referred to the literature.[14]

As shown in Fig. 2, a MCPF with two modules ($N = 2$) is employed in this research to achieve a larger stroke while keeping the parameters l and h unaltered. The benefit of using MCPF lies in that it enables a long positioning range while maintaining a compact physical dimension. To improve the transverse stiffness, the two terminals are connected together as indicated by a dashed line in Fig. 2. By adopting four such MCPFs, a symmetric positioning mechanism is devised and its CAD model is shown in Fig. 3.

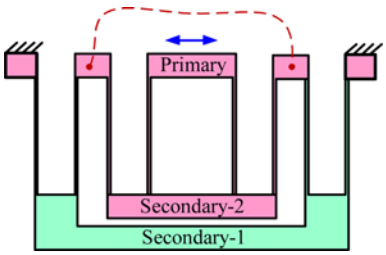

Fig. 2 A MCPF with two modules ($N = 2$)

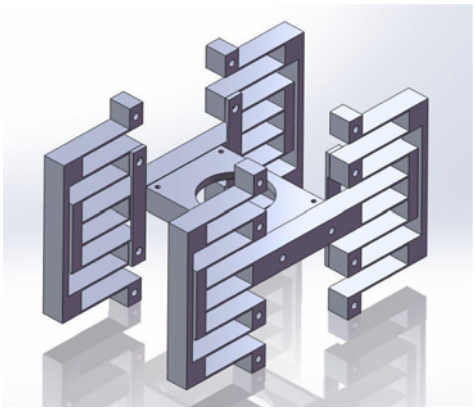

Fig. 3 CAD model of the designed positioning mechanism

2.2 Space arrangement and shape design

Once the positioning mechanism is designed, the components of motor, digital microscope, and positioning mechanism should be arranged and combined properly to construct the auto-focusing function. The shape design is based on some space restriction conditions and physical limitations as listed below.

(1) The whole design should be vertical to the ground to construct an upright microscope system.
(2) The produced output force of the motor should act along the central axis of the multi-stage leaf spring to reduce parasitic errors.
(3) The VCM motor cannot be fixed upside down, because its moving coil will not be held under powerless condition.
(4) The object to be observed should locate under the microscope, because if the object is put upward the microscope, the light may interference the picture. It also means that the microscope also cannot be fixed upside down.
(5) The mass of the VCM motor should not be located on the multi-leaf spring, because it is very heavy that will waste the deformation of the device.

In view of the aforementioned constraint conditions, a design solution is found to solve all of these problems. The motor, positioning mechanism, and digital microscope (not shown) are arranged as depicted in Fig. 4.

As the fixing frame of the device, two plastic boards are used to make the microscope be vertical to the ground. The CAD model in Fig. 4 shows the space arrangement of the main parts. It is seen that a VCM motor of cylinder shape is placed on the motor holder, the holder is supported by two plastic frames. The coil of the motor is connected with a square platform by two screws and four long thin cylindrical bars are used to connect the square platform and the positioning stage together. The central hole of the positioning stage is used to hold the microscope firmly. When the motor creates a displacement, the four bars will drive the stage upward and downward to realize the auto-focusing.

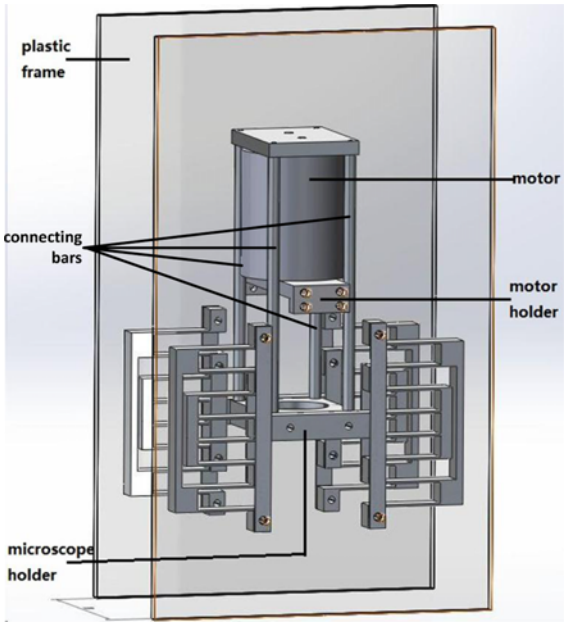

Fig. 4 CAD model of the designed auto-focusing device

Table 1 Specifications of Aluminum 7075

Parameter	Value
Density	2810 kg/m^3
Modulus of elasticity	72 Gpa
Yield strength	455 Mpa
Tensile strength	524 Mpa

3. Analytical Modeling and Optimum Design

To fabricate the positioning mechanism, the material of aluminum 7075 (Al-7075) is selected. This material is a cold forging aluminum alloy which has a higher elasticity than mild steel. It is one of the best commercial alloys now. The specifications of Al-7075 are shown in Table 1.

According to Eq. (9), the motion range of the MCPF with multiple leaf springs can be derived as follows.

$$\Delta x_{max}^{multi} = \frac{4\sigma_{max} l^2}{3hE} \tag{11}$$

where $N = 2$ is used which represents the number of basic modules of each MCPF.

In addition, considering that the output stage of the positioning mechanism is connected to the base through four MCPFs, its stiffness can be calculated as $4K_{multi} = 2Ebh^3 / l^3$, which is derived from Eq. (10).

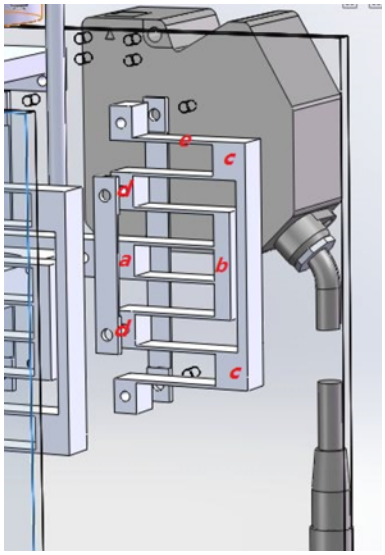

Fig. 5 Different parts of a multi-stage leaf spring

To generate a rapid response, the device should own a high natural frequency. In order to calculate the natural frequency, a dynamics model of the device is established as follows.

3.1 Dynamics modeling

When the multi-stage leaf spring moves, different parts have different velocities. Referring to Fig. 5, assume that the central part a has a velocity $\dot{x}$. Then, part b has a velocity of $3\dot{x}/4$. In addition, part d has a velocity of $2\dot{x}/4$ and part c has a velocity of $\dot{x}/4$.

Extracting the term $\dot{x}$ from the kinetic energy function of parts a, b, c, d, and e (these parts are indicated in Fig. 5), one can get the equation of overall kinetic energy as shown below:

$$E_k = \frac{1}{2} m \dot{x}^2 \tag{12}$$

where the equivalent mass is expressed by

$$m = m_a + 2m_b\left(\frac{3}{4}\right)^2 + 2m_c\left(\frac{1}{4}\right)^2 + 4m_d\left(\frac{2}{4}\right)^2 + 4m_e\left(\frac{1+\frac{3}{4}}{2}\right)^2 + 4m_e\left(\frac{\frac{3}{4}+\frac{2}{4}}{2}\right)^2 + 4m_e\left(\frac{\frac{2}{4}+\frac{1}{4}}{2}\right)^2 + 4m_e\left(\frac{\frac{1}{4}+0}{2}\right)^2 + 24I_e\frac{1}{(4l)^2} \tag{13}$$

where the mass of each part of the multi-stage leaf spring is shown below.

$$m_a = \rho b(2h + 0.009)(0.04 + 2\times 0.007) \tag{14}$$

$$m_b = \rho b(0.005)(3\times 0.009 + 4h) \tag{15}$$

$$m_c = \rho b[0.003(0.01\times 2 + 0.09\times 5 + 8h) + 2(0.007\times(0.009 + 2h))] \tag{16}$$

$$m_d = \rho b \times 0.007 \times (0.009 + 2h) \tag{17}$$

$$m_e = \rho b h l \tag{18}$$

Table 2 Mass values of different parts (unit: kg)

m_a	m_b	m_c	m_d	m_e
0.0201	0.0054	0.0129	0.0026	0.0000591

where ρ is the density of the material and the thickness of the device is selected as b = 10 mm. In addition, the moment of inertia of the part e is shown below:

$$I_e = \frac{m_e \times l^2}{12} \tag{19}$$

Afterwards, the potential energy is calculated through the stiffness K. The dynamic stiffness K_{ds} is derived as:[19]

$$K_{ds} = 2\gamma K_\theta \frac{EI}{l} \tag{20}$$

where γ = 0.85 and K_θ = 2.6686.

The relationship between K and K_{ds} is shown below:[19]

$$K = \frac{32 \times K_{ds}}{(4l)^2} \tag{21}$$

By using Lagrangian equation, the dynamics model can be obtained, and the natural frequency in the free-motion condition is derived as follows.

$$f = \sqrt{\frac{K}{m}} \tag{22}$$

That is,

$$f = \sqrt{\frac{\gamma k_\theta E b h^3}{3l^3\left(m_a + \frac{9}{8}m_b + \frac{1}{8}m_c + m_d + \frac{43}{8}m_e\right)}} \tag{23}$$

3.2 Optimum design

To design the device with the highest natural frequency, two constraints are considered. One is that the displacement should be at least 10 mm, and the other one is that the motor's force should be able to drive the device. After consulting the specifications of the motor, the maximum force is selected as 200 N.

From the analytical models as established above, it is obtained that

$$\frac{4\sigma_{max} l^2}{3hE} - 0.01\text{m} \geq 0 \tag{24}$$

$$200\text{N} - \frac{2Ebh^3 \times 0.005\text{m}}{l^3} \geq 0 \tag{25}$$

Generally, the larger the natural frequency, the rapider response the device will provide. The main design parameters of the device are the length l and width h of the leaf flexures. Concerning the parameter h, it is set less than 1 mm so as to generate sufficiently low stiffness. Then, by consulting with the manufacturing company, it is realized that the wire electrical discharge machining (EDM) processes usually can produce a minimal width of about 0.3 mm. If it is less than 0.3 mm, it will not be stable because of the manufacturing tolerance. So, the range is selected as h [0.0003 m, 0.001 m]. As for the parameter l,

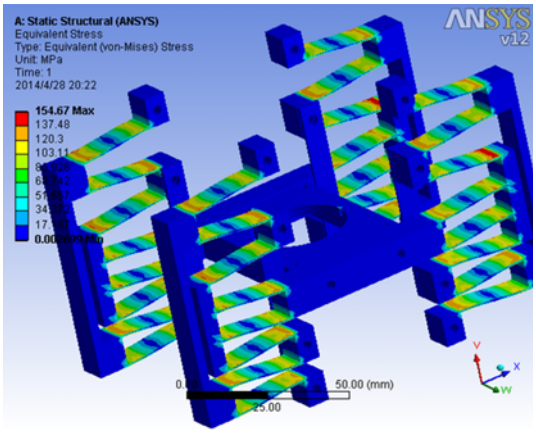

Fig. 6 FEA result of the equivalent (von-Mises) stress distribution

considering the compactness requirement, its range is chosen as l [0, 0.027 m].

By selecting Eq. (23) as the objective function for maximization under the constraints Eqs. (24) and (25) along with two parameter ranges, an optimum design is carried out. Specifically, the optimization is realized by using genetic algorithm (GA) toolbox in MATLAB software. The optimization process is conducted by 20 times, and the best result is selected. That is, the length of flexure $l = 0.027$ m and width of flexure $h = 0.0006$ m. With these parameters, the mass properties are listed in Table 2 and the natural frequency is obtained as 70.20 Hz. The performance of the positioning mechanism is verified by simulation study in the following section.

4. Simulation Study

4.1 Static FEA results

First, static FEA simulation is conducted by applying a force (150 N) on the output platform of the positioning mechanism. The total deformation is generated. It is found that the maximum displacement is already 11.599 mm. Obviously, this displacement is more than enough for the microscope to focus on an object.

In addition, the overall equivalent (von-Mises) stress distribution of the mechanism is shown in Fig. 6. It is seen that the maximum stress occurs around the ends of each leaf spring. Moreover, the maximum stress is less than the yield stress of the material. These results indicate that the designed mechanism satisfies the design requirement.

It is notable that the stress analysis is carried out without considering the stress concentration effect. In the future work, the stress concentration factor will be considered to improve the analytical model (11), and the corner fillet will be adopted to reduce the stress concentration effect. The calculation process of the maximum stress of corner-filleted flexure hinge can be found in the literature[22] and references therein.

4.2 Dynamic FEA results

Second, a modal analysis is performed to examine the dynamic performance of the designed mechanism. The first six natural frequencies are listed in Table 3, and the mode shape of the first resonant mode is shown in Fig. 7. It is found that the first mode shape is attributed to the

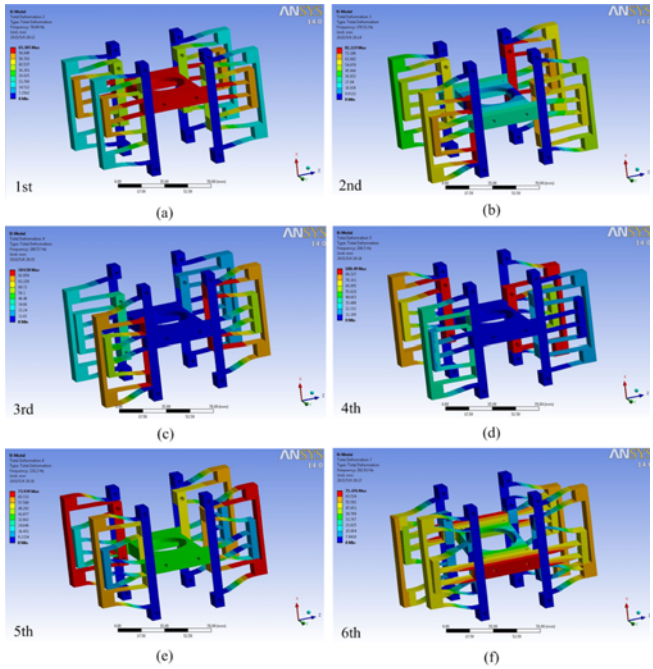

Fig. 7 Simulation results of the first six mode shapes

Table 3 The first-six resonant frequencies of the positioning mechanism

Mode	Frequency (Hz)
1	78.84
2	178.51
3	198.57
4	200.50
5	226.20
6	292.01

working mode at 78.84 Hz. A high natural frequency enables a quick response of the auto-focusing device. In addition, the modes 2 to 5 are caused by the vertical translations of the secondary stages in Z-axis, and the mode 6 is induced by the bending of the output platform around the X-axis.

As compared with the FEA result, the analytical result of the natural frequency is 11% lower. The discrepancy may be caused by the assumption adopted in the analytical process, where only the bending deformations are considered.

The simulation results verify the effectiveness of parametric design of the positioning mechanism. In the next section, a fabricated prototype is described and related experimental results are presented.

5. Prototype Development and Experimental Testing

5.1 Prototype fabrication and assembly

An explosive view of the CAD model of the auto-focusing device is shown in Fig. 8. In addition, a prototype is developed as shown in Fig. 9. The positioning mechanism is manufactured using Al-7075 alloy through the wire EDM process. The VCM provides a stroke of 12.7 mm. The output motion of the device is measured by a laser displacement sensor (model LK-H055, from Keyence Corp.), which provides a

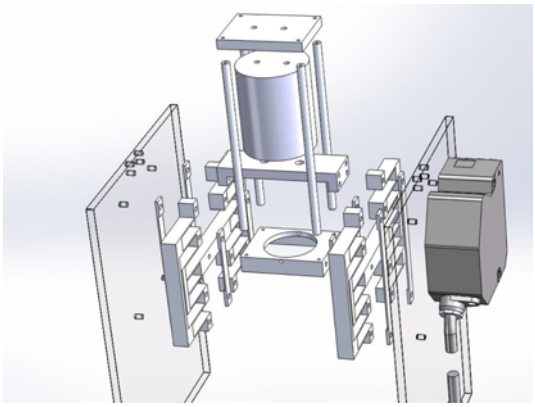

Fig. 8 Explosive view of CAD model of the prototype device

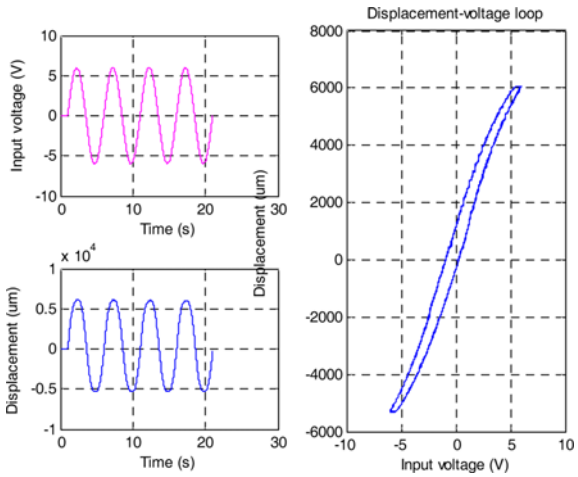

Fig. 10 Motion range testing result of the auto-focusing device

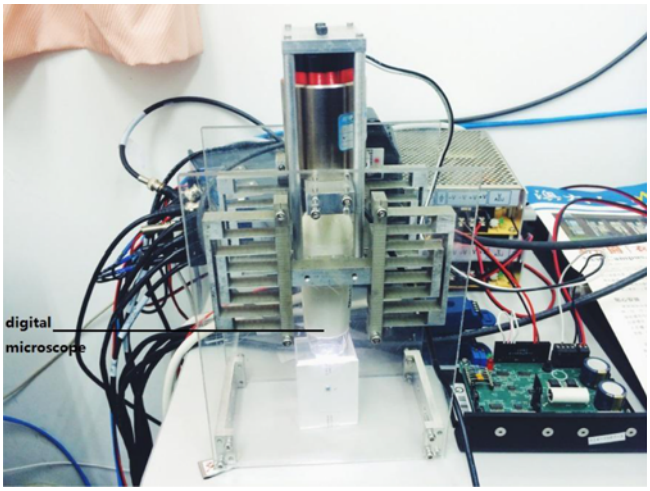

Fig. 9 Experimental device setup

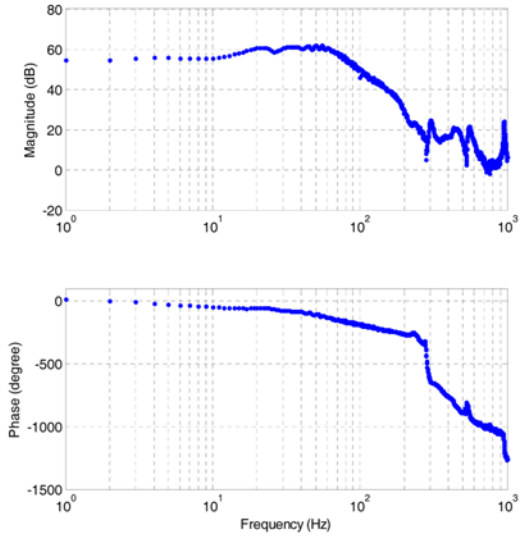

Fig. 11 Bode diagrams of the frequency response of the device

resolution of 25 nm within a measuring range of 20 mm. The digital microscope provides a maximum amplification ratio of 200 with a frame rate of 30 fps. Control algorithm is developed using NI LabVIEW software along with Vision Development Module.

5.2 Experimental testing

First, the motion range is tested by driving the VCM. By applying a 0.5-Hz sinusoidal voltage ranging between -6 to 6 V to the VCM, the result is shown in Fig. 10. It is found that the motion range is about 11.3 mm, which exceeds the design requirement of 10 mm. Moreover, the ANSYS simulation confirms that the range of 11.3 mm is acceptable.

Fig. 10 shows the time histories of the applied voltage and produced displacement as well as the displacement-voltage curve. The displacement-voltage curve exhibits a nonlinear loop, not a straight line. This is because of the hysteresis effect. The hysteresis is mainly caused by the electromagnetic element of the VCM.

Next, the dynamic performance of the device is tested by the frequency response method. Specifically, by applying a swept sine wave with the amplitude of 0.5 V and frequency ranging from 1 to 1000 Hz, the frequency response is generated as shown in Fig. 11. It is observed that a resonant peak occurs around the frequency of 50 Hz, which is smaller than the first resonant frequency predicted by FEA simulation (78.84 Hz). The discrepancy is mainly caused by the masses of the moving coil and connecting bars, which are not considered in the simulation study. The resonant frequency can be improved by reducing the moving mass of the device.

6. Experimental Study of the Auto-Focusing Device

6.1 Auto-focusing algorithms

6.1.1 The feature of an ideal focus curve

Before the auto-focusing, finding a suitable clarity index of the image is the first step, which is one of the most important problems in digital auto-focusing technology.

The basic requirements to an ideal focus-value curve are shown below.

(1) The ideal focus value curve only has a single peak and its maximum corresponding to the clearest image (i.e., the best in-

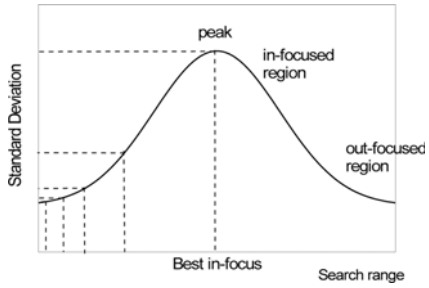

Fig. 12 Ideal focus curve of an image by selecting the standard deviation of the grayscale as clarity index

focus position).

(2) The ideal focus value curve is monotonically increasing when the lens position is approaching the best in-focus position (on the left side of the peak). And the curve is monotonically decreasing when the lens position is far from the best in-focus position (on the right side of the peak).

(3) The influence caused by the noise should be as small as possible.

Fig. 12 shows an ideal focus curve by selecting the standard deviation of the image grayscale as the clarity index. It illustrates the changes of image clarity as the lens position varies. The standard deviation of the curve increases when the lens position is approaching the best in-focus position (on the left side of the peak). Then, the lens position at the peak value of the image standard deviation denotes a best in-focus position. After meeting the best in-focus position, the standard deviation of the curve decreases as the lens getting far from the best in-focus position (on the right side of the peak). Neighborhood of the peak is referred as an in-focus region but far from the peak is referred as an out-focused region.

6.1.2 Focusing and searching algorithms

To realize the auto-focusing of the microscope, the image is acquired and processed to find the focusing position with the clearest image.

Focusing algorithm is an important part in auto-focusing. The current focusing algorithms can be divided into two domains: the spatial domain and frequency domain.[20] In particular, the statistical algorithm uses the variance and correlation to determine whether the image is focused. As compared with other algorithms, the statistical algorithm is less sensitive to the noise of image. Hence, the statistical-based algorithm is selected as focusing algorithm in this research. Specifically, the standard deviation of the grayscale is calculated as the clarity index of the image.

Regarding the searching algorithm, different approaches (e.g., hill-climbing algorithm, Fibonacci search algorithm, approximation theory, exhaustive search, etc.) have been proposed in the literature.[21] Considering that the exhaustive search method is less sensitive to local maximum, it is employed to find the focusing position with the highest value of the clarity index in this research. More details about the advantages and disadvantages of the algorithms can be found in Ref. 21.

6.2 Experimental results

In this work, LabVIEW software with Vision Development Module is adopted for the image processing. The image acquisition and processing procedures are briefly shown as follows.

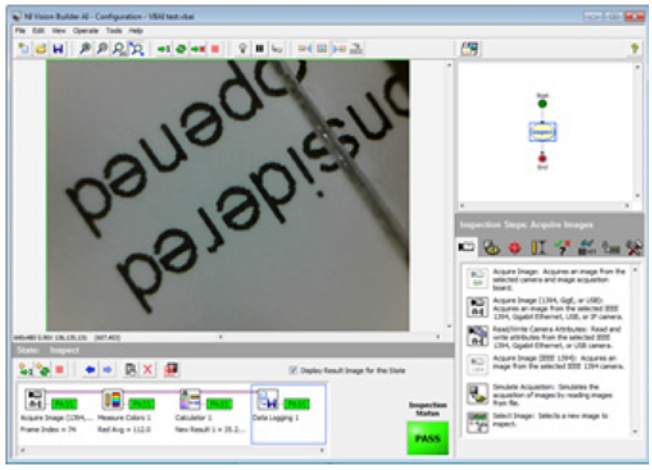

Fig. 13 A snapshot of image processing using LabVIEW software

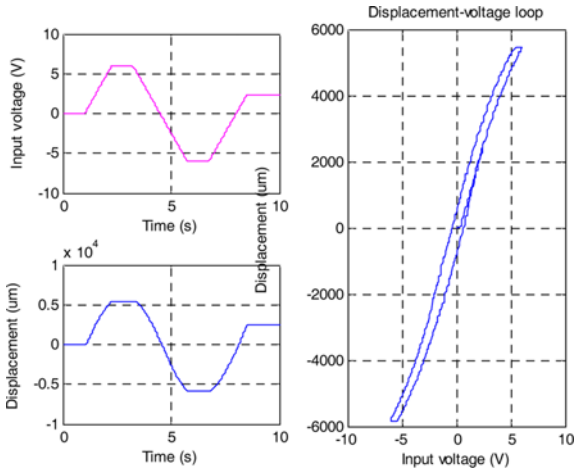

Fig. 14 Experimental result of auto-focusing testing

Step 1: Acquire the RGB image.

Step 2: Measure the histogram of the RGB image.

Step 3: Extract the standard deviation of gray-scale of green (or red or blue) plane.

As a case study, the auto-focusing of a 1-mm object is implemented. A snapshot of image processing using LabVIEW software is shown in Fig. 13. The focusing curves are illustrated in Figs. 14 and 15. It is observed that the device executes a full-range scan first and then stops at the position with the highest clarity index, i.e., maximum standard deviation value, as shown in Fig. 14. The displacement-voltage curve is shown in Fig. 14 (right), which represents a nonlinear hysteresis loop. As mentioned earlier, the hysteresis is mainly caused by the adopted VCM in this work.

Moreover, Fig. 15 indicates that the focusing process exhibits both local and global maxima, which is induced by the hysteresis effect. It is notable that vertical axis in Fig. 15 represents the standard deviation of the image grayscale. The grayscale is an 8-bit integer ranging from 0 (black) to 255 (white). Owing to the advantage of exhaustive search method, the global maximum point can be determined within the focusing range. Finally, the device stops at the position with the global

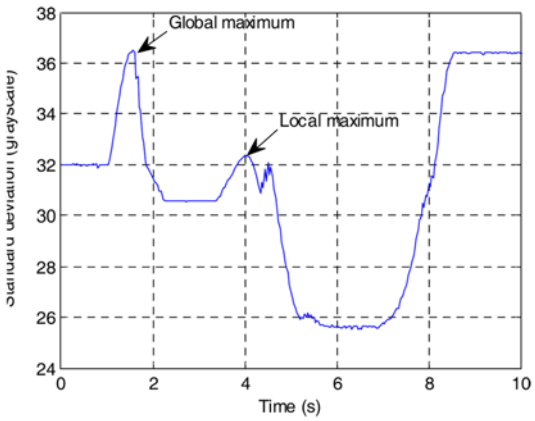

Fig. 15 Standard deviation plot of the image during the auto-focusing process

maximum of clarity index.

The forgoing experimental results reveal that the device stops at the driving point with the maximum standard deviation value, i.e., the clearest image output. The experimental results verify the effectiveness of the developed auto-focusing device. In the future, suitable control technique will be employed to suppress the nonlinearity of the auto-focusing system.

In addition, because the VCM in combination with the flexure mechanism can provide a smooth motion, the focusing resolution is dependent on the resolution of the employed displacement sensor. That is 25 nm in this work. Regarding the total time of focusing cycle, it is determined by the translation speed of the VCM and computational time of the auto-focusing algorithm. In this work, a focusing cycle of 7.5 s is achieved. The focusing time will be further shortened in the future work.

7. Conclusions

This paper presents the design and analysis of a new auto-focusing device for a microscope. As the key part of the device, the positioning mechanism is designed in detail. Analytical models are derived to evaluate the stiffness and resonant frequency of the mechanism. An architectural optimization is carried out to generate a resonant frequency as high as possible. The performance of the designed mechanism is examined by a series of FEA simulation studies. Results demonstrate that the designed positioning mechanism satisfies the design requirement. It delivers a long focusing range over 10 mm for the microscope. Moreover, it allows a rapid response for the auto-focusing device, which is enabled by a high resonant frequency. Afterwards, a prototype is fabricated for experimental testing. In the experimental study, the function of auto-focusing is successfully demonstrated. The focusing criterion is the grey-scale standard deviation value of a green (or red or blue) plane. The global maximum point is searched by the exhaustive search method, which is the best output with the clearest image of the microscope. Experimental results show that the developed auto-focusing device is capable of determining the global optimum focusing point over 10-mm focusing range. In the future work, feedback control will be implemented to achieve a precise control of the auto-focusing device

ACKNOWLEDGEMENT

The work was support by the Macao Science and Technology Development Fund under Grant Nos.: 070/2012/A3 and 052/2014/A1 and the Research Committee of the University of Macau under Grant Nos.: MYRG083(L1-Y2)-FST12-XQS and MYRG078(Y1-L2)-FST13-XQS.

REFERENCES

1. Gauthier, M. and Piat, E., "Control of a Particular Micro-Macro Positioning System Applied to Cell Micromanipulation," IEEE Transactions on Automation Science and Engineering, Vol. 3, No. 3, pp. 264-271, 2006.
2. Liu, X., Wang, Y., and Sun, Y., "Cell Contour Tracking and Data Synchronization for Real-Time, High-Accuracy Micropipette Aspiration," IEEE Transactions on Automation Science and Engineering, Vol. 6, No. 3, pp. 536-543, 2009.
3. Kim, J. H., "Visually Guided 3D Micro Positioning and Alignment System," Int. J. Precis. Eng. Manuf., Vol. 12, No. 5, pp. 797-803, 2011.
4. Kramar, J. A., "Nanometre Resolution Metrology with the Molecular Measuring Machine," Measurement Science and Technology, Vol. 16, No. 11, pp. 2121-2128, 2005.
5. Sinno, A., Ruaux, P., Chassagne, L., Topçu, S., Alayli, Y., et al., "Enlarged Atomic Force Microscopy Scanning Scope: Novel Sample-Holder Device with Millimeter Range," Review of Scientific Instruments, Vol. 78, No. 9, Paper No. 095107, 2007.
6. Polit, S. and Dong, J., "Development of a High-Bandwidth XY Nanopositioning Stage for High-Rate Micro-/Nanomanufacturing," IEEE/ASME Transactions on Mechatronics, Vol. 16, No. 4, pp. 724-733, 2011.
7. Yu, H. C. and Liu, T., "Design of a Slim Optical Image Stabilization Actuator for Mobile Phone Cameras," Physica Status Solidi (C), Vol. 4, No. 12, pp. 4647-4650, 2007.
8. Kim, C., Song, M.-G., Park, N.-C., Park, K.-S., Park, Y.-P., and Song, D.-Y., "Design of a Hybrid Optical Image Stabilization Actuator to Compensate for Hand Trembling," Microsystem Technologies, Vol. 17, No. 5-7, pp. 971-981, 2011.
9. Choi, K.-B., Lee, J. J., Kim, G. H., and Lim, H. J., "A Compliant Parallel Mechanism with Flexure-based Joint Chains for Two Translations," Int. J. Precis. Eng. Manuf., Vol. 13, No. 9, pp. 1625-1632, 2012.
10. Xu, Q. and Li, Y., "Analytical Modeling, Optimization and Testing of a Compound Bridge-Type Compliant Displacement Amplifier," Mechanism and Machine Theory, Vol. 46, No. 2, pp. 183-200, 2011.

11. Tian, Y., Shirinzadeh, B., Zhang, D., Liu, X., and Chetwynd, D., "Design and Forward Kinematics of the Compliant Micro-Manipulator with Lever Mechanisms," Precision Engineering, Vol. 33, No. 4, pp. 466-475, 2009.

12. Song, M.-G., Baek, H.-W., Park, N.-C., Park, K.-S., Yoon, T., et al., "Development of Small Sized Actuator with Compliant Mechanism for Optical Image Stabilization," IEEE Transactions on Magnetics, Vol. 46, No. 6, pp. 2369-2372, 2010.

13. Kim, C., Song, M.-G., Kim, Y., Park, N.-C., Park, K.-S., et al., "Design of an Auto-Focusing Actuator with a Flexure-based Compliant Mechanism for Mobile Imaging Devices," Microsystem Technologies, Vol. 19, No. 9-10, pp. 1633-1644, 2013.

14. Xu, Q., "New Flexure Parallel-Kinematic Micropositioning System with Large Workspace," IEEE Transactions on Robotics, Vol. 28, No. 2, pp. 478-491, 2012.

15. Jeong, J.-H., Kim, M.-H., Woo, S., Gweon, D.-G., Ahn, D., and Hong, D., "Design of a Six-Degree-of-Freedom Motion Fine Stage Driven by Voice Coil Motors with Flexural Guides," Int. J. Precis. Eng. Manuf., Vol. 16, No. 1, pp. 203-207, 2015.

16. Jung, J.-K., Youm, W.-S., and Park, K.-H., "Vibration Reduction Control of a Voice Coil Motor (VCM) Nano Scanner," Int. J. Precis. Eng. Manuf., Vol. 10, No. 3, pp. 167-170, 2009.

17. Yong, Y. K., Lu, T.-F., and Handley, D. C., "Review of Circular Flexure Hinge Design Equations and Derivation of Empirical Formulations," Precision Engineering, Vol. 32, No. 2, pp. 63-70, 2008.

18. Mohammad, T. and Salisbury, S., "Design Considerations for Long Travel Z-Axis Ultra-Precision Positioning Stage," Int. J. Precis. Eng. Manuf., Vol. 13, No. 9, pp. 1581-1588, 2012.

19. Xu, Q., "Design, Testing and Precision Control of a Novel Long-Stroke Flexure Micropositioning System," Mechanism and Machine Theory, Vol. 70, pp. 209-224, 2013.

20. Yu, M. Y., Han, M. L., Shee, C. Y., and Ang, W. T., "Autofocusing Algorithm Comparison in Bright Field Microscopy for Automatic Vision Aided Cell Micromanipulation," Proc. of IEEE 4th International Conference on Nano/Molecular Medicine and Engineering (NANOMED), pp. 88-92, 2010.

21. Sun, Y., Duthaler, S., and Nelson, B. J., "Autofocusing in Computer Microscopy: Selecting the Optimal Focus Algorithm," Microscopy Research and Technique, Vol. 65, No. 3, pp. 139-149, 2004.

22. Lobontiu, N., Paine, J. S., Garcia, E., and Goldfarb, M., "Corner-Filleted Flexure Hinges," Journal of Mechanical Design, Vol. 123, No. 3, pp. 346-352, 2001.